




Original Paper

Highly efficient TiO₂-pillared smectite clay with Ni and Co doping for Rhodamine B removal: kinetics of adsorption and photodegradation

Adi Darmawan , Setyo Sulaksono, Muhamad Samsul Arifin, Hasan Muhtar  and Sriyanti Sriyanti 

Department of Chemistry, Diponegoro University, Tembalang, Semarang, Indonesia

Abstract

Clay exhibits the capability to adsorb dyes such as Rhodamine B (RhB); practical application reveals its susceptibility to desorption, however, compromising its efficacy for RhB removal. To address this concern, modification of Natural Boyolali Region Clay (NBR Clay) was conducted by introducing TiO₂ pillars and incorporating Co and Ni as dopants. This modification aimed to augment the clay's photodegradation capability and its RhB removal capacity. The principal objective of this study was to assess the characteristics of TiO₂-pillared clay doped with Co and Ni and to evaluate its effectiveness in RhB removal. The prepared samples were analyzed using Fourier-transform infrared spectroscopy (FTIR), X-ray diffraction (XRD), thermogravimetric analysis with differential scanning calorimetry (TGA-DSC), and gas sorption analysis (GSA). TGA results indicated stability for all samples up to 650°C, except for Co-Ti/NBR Clay. After 2.5 min, the adsorption capacity of both NBR Clay and NBR Clay+ethanol (EtOH) significantly surpassed that of Ti/NBR Clay, Ni-Ti/NBR Clay, and Co-Ti/NBR Clay. However, the adsorption energy of Ti/NBR Clay, Ni-Ti/NBR Clay, and Co-Ti/NBR Clay exceeded that of NBR Clay and NBR Clay+EtOH. Furthermore, all samples adhered to the Langmuir isotherm model, indicative of a physisorption mechanism. Notably, after 80 min, the percentage of photocatalytic degradation for plain clay reached 99.61%, and this value increased with the introduction of TiO₂ and doping. The Co-Ti/NBR Clay sample exhibited the highest degradation rate at 99.97%. These findings underscore the favorable influence of TiO₂ addition and doping on enhancing RhB removal efficiency.

Keywords: cobalt doping; nickel; Rhodamine B; TiO₂-pillared clay

(Received: 08 January 2024; revised: 11 January 2024; accepted: 12 January 2024)

Introduction

Textile waste produced by the dyeing industry has the potential to pollute the environment. The existence of textile waste in water can interfere with the penetration of sunlight. As a result, the life of organisms in the waters is disrupted, and at the same time, it can threaten the sustainability of aquatic ecosystems (Khan et al., 2023). On the other hand, dye waste produced from the textile industry is generally a non-biodegradable organic compound, which is a cause of environmental pollution, especially in the aquatic environment. One dye often used in the textile industry is Rhodamine B (RhB) (Van Hoang et al., 2022). RhB is a basic dye that is important in the coloring process in the textile and paper industries. However, RhB is of particular concern because its aromatic structure of RhB is difficult to degrade. The impacts include skin and eye irritation, digestive tract disorders, and shortness of breath.

Several types of materials are used in an effort to remove RhB, one of which is clay. Characteristics of the clay surface, such as structure, ion exchange capacity, specific surface area, mechanochemical

stability, water-holding capacity, and surface reactivity means that clays have significant potential in terms of RhB removal (Eren, 2010). Although the adsorption process is considered simple, it has limitations: the limited adsorption capacity of the adsorbent and the possibility of desorption mean that improvement and modification of clay is required (Tretiak et al., 2009).

Efforts have been made to improve the ability to remove RhB from clay using clay pillarization with TiO₂ through a photodegradation process (Yamanaka et al., 1987). TiO₂ is a photocatalyst material capable of degrading RhB with the help of ultraviolet radiation (Dao et al., 2021). TiO₂ is studied and used in many applications because of its strong oxidizing ability to decompose organic pollutants, high hydrophilicity, high chemical stability, long shelf life, non-toxicity, low cost, and transparency to visible light (Nakata et al., 2012). TiO₂ splinting of clay also has other advantages. Unstable interlayer structures in clay and loss of porosity due to heating at high temperatures can be overcome by inserting ions or molecules into the interlayer, known as intercalation. Heating the intercalation substance produces pillars, better known as pillarization (Pinnavaia, 1983). By making pillared clay, the area between layers becomes more stable due to metal oxides forming pillars in the area between layers (Najafi et al., 2021).

Using TiO₂ as a photocatalyst presents a weakness – its wide bandgap energy of 3.23 eV. To address this, innovative approaches

Corresponding author: Adi Darmawan; Email: adidarmawan@live.undip.ac.id

Cite this article: Darmawan A., Sulaksono S., Arifin M.S., Muhtar H., & Sriyanti S. (2024). Highly efficient TiO₂-pillared smectite clay with Ni and Co doping for Rhodamine B removal: kinetics of adsorption and photodegradation. *Clays and Clay Minerals* 72, e7, 1–11. <https://doi.org/10.1017/cmn.2024.12>

have been explored, including narrowing the bandgap energy (E_g) (Abdo Segne et al., 2011) through the insertion (doping) of metals and non-metals. Numerous studies have demonstrated that doping TiO_2 with transition metals like Fe (Sukhadeve et al., 2022), Co (Basumatary et al., 2023), Ni (Santos et al., 2023), Au, and Ag (Zhang et al., 2023) can decrease E_g values, enhancing photocatalytic activity. These transition metal dopants in TiO_2 act as electron trappers, augmenting the separation of electron-hole pairs and, consequently, increasing the photocatalytic efficiency of TiO_2 (Zhou et al., 2020). Nickel and cobalt, among the transition metals, are particularly effective dopants for TiO_2 . Ni doping reduces the bandwidth from 3.28 to 2.7 eV (Opra et al., 2021), while Co doping reduces the bandgap from 3.11 to 2.94 eV (El Mragui et al., 2021). The presence of nickel and cobalt metal ion doping is anticipated to extend the photoresponse of TiO_2 into the visible spectrum, enabling its application in the degradation of colored organic contaminants and other pollutants (Sun et al., 2014). The research hypothesis posits that modifying clay with TiO_2 , coupled with nickel or cobalt doping, enhances adsorption capacity for RhB removal. The insertion of nickel or cobalt metal ions is expected to narrow the energy band gap of TiO_2 , thereby boosting its photocatalytic efficiency. This study aims to extend the photolysis response of TiO_2 to the visible range, providing an effective and environmentally friendly method for removing RhB from waste water.

This investigation builds upon prior research conducted by Cardona et al. (2022) concerning the synthesis of TiO_2 -pillared clay for the degradation of organic compounds. The incorporation of nickel or cobalt doping represents a distinctive aspect of the research, with particular emphasis on their application for the removal of RhB dyes. Comprehensive analysis and characterization of the samples were conducted using FTIR, TGA-DSC, XRD, and GSA. The investigation also encompassed an examination of the adsorption and photodegradation activities of RhB by the samples, including an exploration of their kinetics and thermodynamics.

Materials and methods

Materials

The raw clay used was taken directly from the Wonosegoro District, Boyolali Regency, Central Java Province, Indonesia. $\text{Ni}(\text{NO}_3)_2 \cdot 6\text{H}_2\text{O}$ (AR, 99%), $\text{Co}(\text{NO}_3)_2 \cdot 6\text{H}_2\text{O}$ (AR, 99%), ethanol (AR, 98%), and Rhodamine B (AR, 99%) were purchased from Merck Co., Germany, while TiCl_4 (AR, 98%) was purchased from Sigma-Aldrich Co., USA.

Clay preparation

The Natural Boyolali Region (NBR) clay was washed with water to remove impurities and then dried. The clay was crushed and sieved with a 170-mesh sieve to obtain a smaller clay size and used as the first sample. 10 g of NBR clay was added to 44 mL of ethanol (Clay+EtOH).

Pillarization of titania on NBR clay

10 mL of TiCl_4 solution was added to 44 mL of ethanol and stirred using a magnetic stirrer until homogeneous. 10 g of NBR clay was poured into the titania pillar solution slowly while stirring with a magnetic stirrer at room temperature for 24 h until homogeneous. The NBR clay was washed using ethanol, then dried, crushed, and sieved with a 170-mesh sieve, and calcined at 300°C for 2 h. This sample was referred to as Ti/NBR Clay.

Titania-pillared NBR Clay doped with Ni^{2+} and Co^{2+}

10 mL of TiCl_4 solution was added to 44 mL of ethanol and stirred using a magnetic stirrer; 2.9 g of $\text{Ni}(\text{NO}_3)_2 \cdot 6\text{H}_2\text{O}$ or $\text{Co}(\text{NO}_3)_2 \cdot 6\text{H}_2\text{O}$ powder was then added to the pillar solution and stirred using a magnetic stirrer for 24 h. 10 g of NBR clay was poured into the titania pillar solution doped with Ni^{2+} or Co^{2+} while stirring with a magnetic stirrer at room temperature for 24 h and then washed using ethanol. It was then dried, crushed, and sieved with a 170-mesh sieve, and calcined at 300°C for 2 h. These pillared clays are referred to as Ni-Ti/NBR Clay and Co-Ti/NBR Clay.

Characterization

Several techniques and instruments were used to characterize the five samples (Clay, Clay+EtOH, Ti/NBR Clay, Ni-Ti/NBR Clay, and Co-Ti/NBR Clay). The FTIR analysis was performed over the wavenumber range 600–1600 cm^{-1} using a Perkin Elmer Spectrum IR instrument version 10.6.1. The TG/DTA was conducted in a nitrogen atmosphere (100 mL min^{-1}) at a heating rate of 5°C min^{-1} using an STD-Q600 thermal analyzer. The XRD patterns were obtained using an XRD-7000 instrument (Shimadzu) with $\text{CuK}\alpha$ source radiation at a scanning speed of 3°2 θ min^{-1} over the range 3 to 90°2 θ with a source voltage of 30 kV and a current of 30 mA. For GSA analysis, the samples were degassed using a vacuum for a minimum of 6 h at 150°C. GSA analysis was carried out at a temperature of 77K and a pressure of 1 bar. The Brunauer, Emmett and Teller (BET) method was used to determine the specific surface area, while the total pore volume was taken from the last point of the isotherm. The average pore diameter was determined by the 4V/A method according to BET.

RhB removal

RhB adsorption was carried out in the dark (without UV light), while the photocatalytic degradation study was done using UV light. A 0.1 g sample was dispersed into 50 mL of 40 ppm RhB solution with contact times of 2.5, 5, 7.5, 10, 15, 20, 40, and 80 min in the dark room. In addition, it was also applied with variations in RhB concentrations of 5, 10, 20, 40, and 80 ppm. The photocatalytic degradation study was conducted by dispersing 0.1 g of sample into 50 mL of 40 ppm RhB solution for 10 min in a dark room. Then the mixture was removed and irradiated with a UV lamp (15 Watts) with variations of time: 2.5, 5, 7.5, 10, 15, 20, 40, and 80 min. In addition, it was also applied with variations in RhB concentrations of 5, 10, 20, 40, and 80 ppm. After the process, the mixture was centrifuged to separate the product using a clay catalyst. The product formed was then analyzed using a UV-Vis spectrometer, and the absorbance value was measured.

Results and Discussion

Characterization

Functional group

The functional groups of NBR Clay, NBR Clay+EtOH, Ti/NBR Clay, Ni-Ti/NBR Clay, and Co-Ti/NBR Clay were analyzed by FTIR. The spectra (Fig. 1) describe the absorbance over the range 600–1600 cm^{-1} , a distinct region for clay structures (Borno and Ashraf, 2023). All spectra show high and wide peaks at wavenumbers 1039–1050 cm^{-1} , indicating Si–O or Al–O (stretching) groups in Si–O–Si or Al–O–Si (Zhirong et al., 2011).

All spectra showed a similar shape, indicating that the addition of Ti^{4+} or doping of Ni^{2+} and Co^{2+} did not significantly change the chemical environment.

In NBR Clay there is a small peak at wavenumber 880 cm^{-1} , which is lost after the addition of Ti^{4+} pillar solution. This peak shows the vibration of the OH group bending the Si–OH or Al–OH bonds (Sarier et al., 2010). The loss of the 880 cm^{-1} peak indicates a reduction or loss of the OH group in the Si–OH or Al–OH bonds (Yusuf, 2023). This result might happen because Ti^{4+} interacts with the OH group, so the Si–OH or Al–OH bonds weaken and form $\text{Ti}(\text{OH})_4$ (Yan et al., 2010).

A broad peak at wavenumber $\sim 1420\text{ cm}^{-1}$ in clay is the bending vibration of hydroxyl and water molecules in the interlayer region. The peak disappears after the addition of Ti^{4+} . The loss of this peak is caused by dehydration as water molecules are replaced by Ti^{4+} (Zhang et al., 2013). Figure 1 shows that with the addition of ethanol and Ti^{4+} , the $980\text{--}1050\text{ cm}^{-1}$ peaks experienced band separation, as indicated by the appearance of a shoulder at $\sim 1030\text{ cm}^{-1}$. It is suspected that Ti^{4+} strengthens the stretching vibrations on Si–O, where the O atoms are simultaneously tetrahedral and octahedral layers perpendicular to the layer formation (Karakassides et al., 1999). The presence of a small shoulder and peak at $\sim 1110\text{ cm}^{-1}$ indicates the formation of an asymmetric vibration on Si–O, which is tetrahedral in shape (Ouidri and Khalaf, 2009).

Assuming that the FTIR absorption band results from the resonance of the absorption bands of each wavenumber, deconvolution of the FTIR spectra was performed using *Fityk* software to determine band changes. The deconvolution results are presented in Fig. S1 (Supplementary material). There was a change in the shape of the derivation peak from the NBR Clay to NBR Clay+EtOH. Derivative curves 3 ($900\text{--}930\text{ cm}^{-1}$) and 4 ($1000\text{--}1030\text{ cm}^{-1}$) show the functional groups Si–OH or Al–OH and Si–O–Si or Al–O–Si, respectively. In NBR Clay+EtOH, there is a reduction in the area of the derivation curve 3, and the area ratio between the derivation curves 3 and 4 decreases. This result indicates that adding ethanol reduces the presence of Si–OH or Al–OH. In particular, the ratio of the relationship between the areas of the derivation curves 3 to 4 is presented in Fig. 2. The area ratio of Ti/NBR Clay is greater than that of Ni-Ti/NBR Clay and Co-Ti/NBR Clay, indicating that adding doped Ni^{2+} and Co^{2+} reduces the

Si–OH functional groups or Al–OH in an alumina silicate framework.

Thermal analysis

Thermal stability analysis was carried out using TGA-DSC. The results of the analysis (Fig. 3) show that the decomposition reaction occurring in the sample can be explained in three stages: (a) $50\text{--}150^\circ\text{C}$, (b) $150\text{--}650^\circ\text{C}$, and (c) $650\text{--}1000^\circ\text{C}$.

In the first range (I) at a temperature of $50\text{--}150^\circ\text{C}$, there is a reduction in mass for all of NBR Clay, NBR Clay+EtOH, Ti/NBR Clay, Ni-Ti/NBR Clay, and Co-Ti/NBR Clay. The NBR Clay+EtOH has a more significant weight loss than the clay. This is because, in the NBR Clay+EtOH, the compound that evaporates is water and ethanol, while in the clay, the only compound that evaporates is water. Ti/NBR Clay has a more significant mass loss than NBR Clay +EtOH and NBR Clay. This is because the compounds that evaporate in the Ti/NBR Clay are water, ethanol, and Cl^- ions, where the Cl^- ions come from the TiCl_4 compound. The Co-Ti/NBR Clay has the most significant mass loss. This is because, in addition to the evaporation of water, ethanol, and Cl^- ions, water decomposition occurs from $\text{Co}(\text{NO}_3)_2 \cdot 6\text{H}_2\text{O}$ to $\text{Co}(\text{NO}_3)_2 \cdot 3\text{H}_2\text{O}$. However, the decrease for the Ni-Ti/NBR Clay was not as great as that for Co-Ti/NBR Clay because $\text{Ni}(\text{NO}_3)_2 \cdot 6\text{H}_2\text{O}$ did not experience decomposition. The mass loss in Co-Ti/NBR Clay is the largest, $\sim 7.01\%$, then 2.28% for Ni-Ti/NBR Clay, 1.67% for Ti/NBR Clay, 1.51% for NBR Clay+EtOH, and 1.43% for NBR clay.

The second range (II) covers $150\text{--}650^\circ\text{C}$; the four samples did not experience a sharp decrease in mass because only dehydration or water loss occurred. This water-loss process requires temperatures of $>100^\circ\text{C}$ as water is in the area between the clay layers (Ahmad et al., 2013). The mass loss in Co-Ti/NBR Clay was 6.21% , for Ni-Ti/NBR Clay it was 0.84% , for Ti/NBR Clay it was 0.04% , for NBR Clay+EtOH it was 0.17% , and for Clay it was 0.26% . The sharp decrease in Co-Ti/NBR Clay was due to nitrate decomposition. This nitrate comes from $\text{Co}(\text{NO}_3)_2$, where the nitrate group does not participate in the reaction in the doping process, so it is decomposed during the calcination process (Kumar et al., 2016). However, nitrate decomposition in $\text{Ni}(\text{NO}_3)_2$ is less extensive than in $\text{Co}(\text{NO}_3)_2$. This is because the nitrate bond with nickel is stronger than with cobalt.

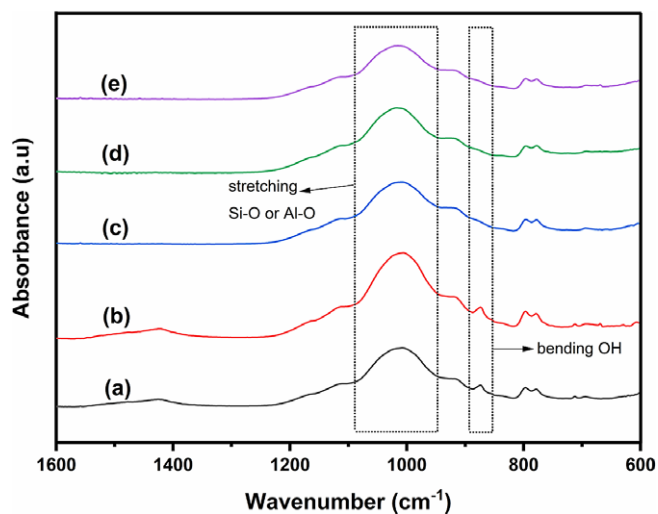


Figure 1. FTIR spectra for (a) Clay, (b) Clay+EtOH, (c) Ti/NBR Clay, (d) Ni-Ti/NBR Clay, and (e) Co-Ti/NBR Clay.

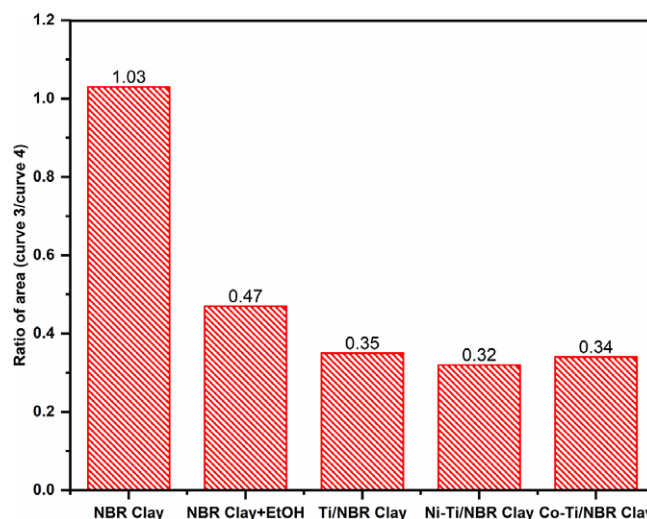


Figure 2. The ratio of the area of curve 3 to the area of curve 4.

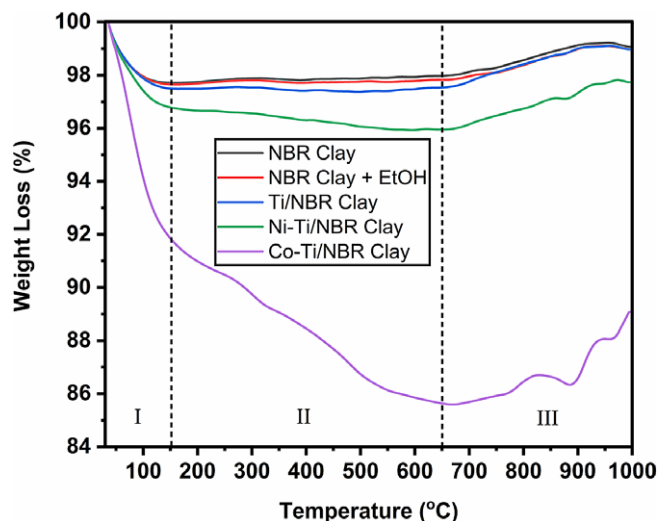


Figure 3. TGA thermograms for Clay, Clay+EtOH, Ti/NBR Clay, Ni-Ti/NBR Clay, and Co-Ti/NBR Clay.

The third range (III) is at temperatures of $>650^{\circ}\text{C}$. At this stage, weight was increased in all samples, marked by an increase in relative mass. This increase may be due to a reaction between the sample and the oxygen gas in the sweeping gas during the TGA analysis. Samples that react with oxygen produce oxides that stoichiometrically give heavier yields (Starink, 2003). This reaction with oxygen occurs due to use of air as a sweeping gas (Laboureur et al., 2019).

This TGA analysis is supported by the DSC data shown in Fig. 4, and shows the relationship between temperature and heat flow. As with TGA, DSC also explains the occurrence of reaction changes which are described in four stages: (a) $30\text{--}150^{\circ}\text{C}$, (b) $150\text{--}500^{\circ}\text{C}$, (c) $500\text{--}700^{\circ}\text{C}$, and (d) $700\text{--}800^{\circ}\text{C}$. In the first stage, the temperature is $30\text{--}150^{\circ}\text{C}$, and an endothermic reaction or heat absorption process occurs in all samples. This can be seen from the downward curve. This endothermic reaction occurs when water and ethanol evaporate in the clay (Bahranowski et al., 2015). The heat absorption is 164.72 , 200.13 , 158.44 , 112.27 , and 118.19 J g^{-1} , respectively, for the NBR Clay, NBR Clay+EtOH, Ti/NBR Clay, Ni-Ti/NBR Clay, and Co-Ti/NBR Clay.

In the second stage, the temperature is $150\text{--}500^{\circ}\text{C}$, and an exothermic reaction or heat release occurs in all samples, which is marked by an increasing curve. This exothermic reaction occurs because the clay has experienced shrinkage. The heat release is 1339.95 , 259.12 , 93.28 , 122.77 , and 60.09 J g^{-1} , respectively, for NBR Clay, NBR Clay+EtOH, Ti/NBR Clay, Ni-Ti/NBR Clay, and Co-Ti/NBR Clay.

In the third stage, at $500\text{--}700^{\circ}\text{C}$, an endothermic reaction occurs in NBR Clay, NBR Clay+EtOH, Ti/NBR Clay, Ni-Ti/NBR Clay, and Co-Ti/NBR Clay. This reaction occurs as there is further shrinkage caused by burning at high temperatures (Zhang et al., 2022). For NBR clay, heat absorption is 189.07 J g^{-1} ; for NBR Clay+EtOH, it is 153.22 J g^{-1} ; for Ti/NBR Clay, it is 245.05 J g^{-1} ; for Ni-Ti/NBR Clay, it is 127.11 J g^{-1} , and for Co-Ti/NBR Clay it is 80.57 J g^{-1} .

At temperatures between 700 and 800°C , there is a clear difference between the clay before and after being pillared with TiO_2 . In the Clay and NBR Clay+EtOH, there are depressions. However, after pillaring with TiO_2 , the concavity disappeared. The DSC appears to peak at 800°C , indicating Ti metal presence (Bahranowski et al., 2015), so it can be assumed that the loss of the

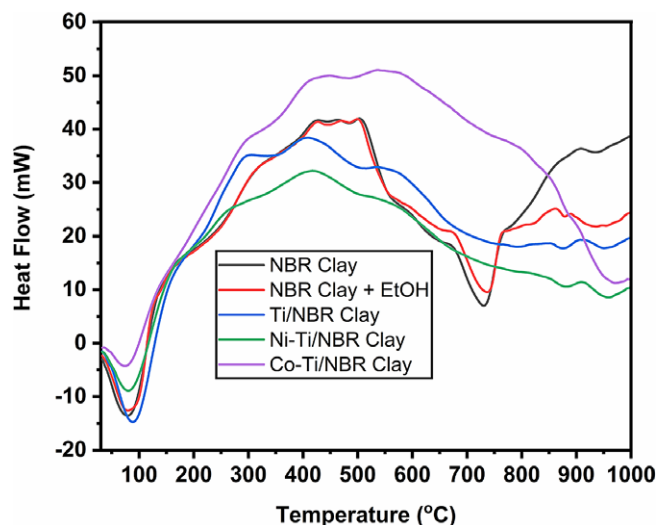


Figure 4. DSC thermogram of titania-pillared clay doped with nickel and cobalt.

depression is due to the presence of Ti metal. From the TGA-DSC, titania-pillared clay is stable at 650°C , because the calcination temperature above 650°C causes the clay to collapse. However, the calcination temperature is $<650^{\circ}\text{C}$, leaving organic impurities.

Crystal structure

All samples obtained were characterized using XRD. Figure 5 presents the XRD patterns of clay and pillared clay. There is a low-intensity peak at $<10^{\circ}2\theta$ which indicates that NBR Clay is a smectite-type clay. Additionally, peaks appear at 19.35 and $62^{\circ}2\theta$ which are characteristic of the mineral montmorillonite. However, the presence of sharp peaks at 26.6 and $21^{\circ}2\theta$, characteristic of quartz, indicates that NBR clay is not pure but mixed with quartz. Although separation was carried out initially, this process cannot wholly separate montmorillonite from quartz. In addition, a broad peak in the range $5\text{--}10^{\circ}2\theta$ indicates the d_{001} plane (Costache et al., 2006). Peaks were observed at 5.66 , 8.76 , 9 , and $8.82^{\circ}2\theta=5.66$ with d_{001} values of 15.72 \AA , 10.095 \AA , 9.875 \AA , and 10.029 \AA , respectively for each of NBR Clay, Ti/NBR Clay, Ni-Ti/NBR Clay, and Co-Ti/NBR Clay. For NBR Clay+EtOH, there is no visible peak in the $<10^{\circ}2\theta$ region. A peak at $5.66^{\circ}2\theta$ in clay is due to interlayer cations (Na^+ or Ca^{2+}), which are hydrated by water so that they can enlarge the galleries between layers. Meanwhile, ethanol is an organic solvent that does not cover interlayer ions well. As a result, the interlayers are not open enough. In addition, ethanol is more volatile and is not bound too tightly to clay. As a result, there is no liquid in the spaces between layers, resulting in reduced interlayer sizes. The XRD pattern also shows that the d_{001} peak is always broad unlike that at $26.6^{\circ}2\theta$. This indicates that the clay layer is amorphous and not crystalline. The sharp peak, at $26.6^{\circ}2\theta$, is not from clay but from quartz mixed in the clay. These results indicate that quartz mixes evenly in the clay.

Figure 5 also shows that there is a shift in the d_{001} peak from $5.66^{\circ}2\theta$ on clay to 8.76 , 9 and $8.82^{\circ}2\theta$ for Ti/NBR Clay, Co-Ti/NBR Clay and Ni-Ti/NBR Clay, respectively, with d_{001} values of 10.095 \AA , 9.875 \AA , and 10.029 \AA . The clay peak shift to larger 2θ values (smaller d_{001} values) indicates that the pillarization process was successful. NBR Clay heated at $>200^{\circ}\text{C}$ loses water, and the area between the clay layers shrinks, so there is no d_{001} peak at $<10^{\circ}2\theta$

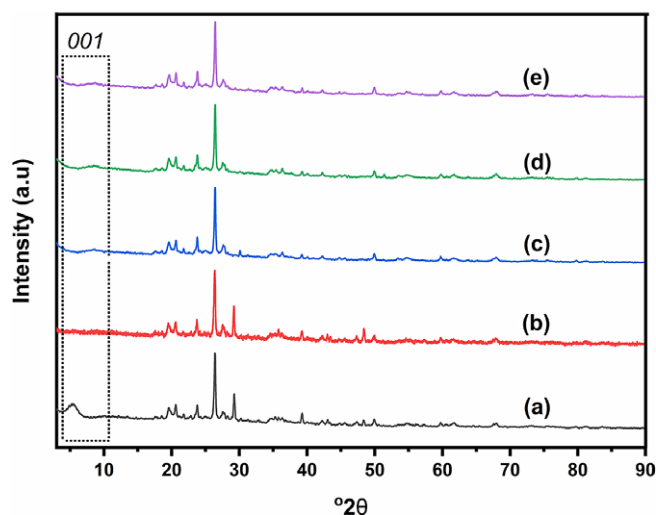


Figure 5. XRD patterns of (a) Clay, (b) NBR Clay+EtOH, (c) Ti/NBR Clay, (d) Co-Ti/NBR Clay, and (e) Ni-Ti/NBR Clay.

(Johnson and Post, 2006). However, the existence of pillars can maintain the existence of interlayer areas. The presence of the d_{001} peak after the addition and calcination of Ti^{4+} indicates that cation exchange occurs where the interlayer clay cations are replaced by Ti^{4+} to further turn into TiO_2 oxide during the calcination (Li et al., 2015). TiO_2 is what becomes a pillar in the area between layers. However, the d_{001} produced by TiO_2 pillars is not as big as d_{001} in natural clay.

The 2θ values for Ni-Ti/NBR Clay and Co-Ti/NBR Clay are similar to those for Ti/NBR Clay. These results indicate that adding Co^{2+} and Ni^{2+} does not affect the size of d_{001} . It can be said that the size of the pillars is the same so the pillars forming only come from Ti^{4+} . Ni^{2+} and Co^{2+} only stick or are in the interlayer cavities of NiO and CoO (and so do not bind with Si–O–Si).

Surface character

Isothermic analysis determines pore volume, surface area, and pore distribution on a micro- or meso-scale. The results of the analysis (Fig. 6) show that the adsorption–desorption curves of all samples are close to type IV, which characterizes mesoporous materials, and the presence of hysteresis of all samples indicates type H4, which implies that the sample has pores with narrow gaps with unusual properties, weak interaction state with adsorbate and has a porous adsorbent (ALothman, 2012). The H4 type implies the formation of capillary condensation in the clay pores, and the H4 type is characteristic of montmorillonite minerals (Zhu et al., 2009).

Figure 6 also shows that the amount of adsorbed nitrogen increases with pillarization with Ti^{4+} and doping with Co^{2+} and Ni^{2+} . This shows that the pillarization process increases the adsorption capacity of the clay due to the expansion of the galleries in the interlayer area due to the formation of pillars. The increase in adsorption may also be caused by the strong interaction between TiO_2 and nitrogen gas, so the amount of adsorbed nitrogen increases.

Table 1 shows that the pore diameter does not show significant variation. The average pore diameter ranges from 40 to 59 Å, while the surface area and pore volume tend to show the same pattern. This means that the pillarization process does not cause changes in pore size. This also indicates that the height of the TiO_2 pillars is fixed and uniform in all layers of the interlayer space. The increase

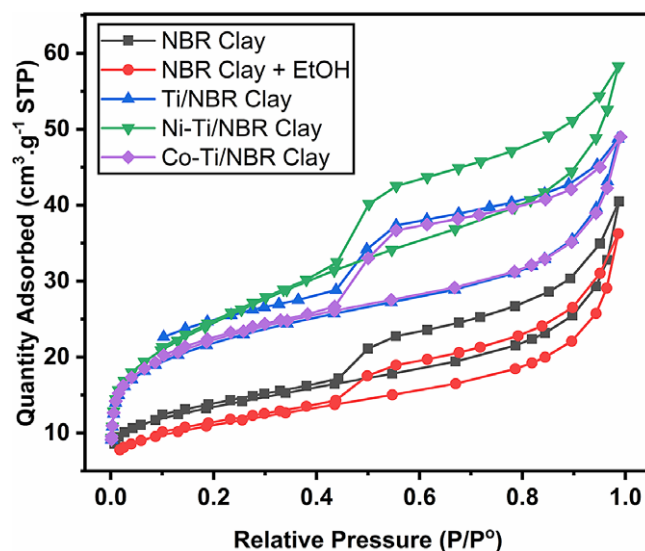


Figure 6. Adsorption–desorption curves of Clay, Clay+EtOH, Ti/NBR Clay, Ni-Ti/NBR Clay, and Co-Ti/NBR Clay.

in pore diameter for Clay of 54 Å to NBR Clay+EtOH of 58.5 Å was caused more by the expansion of the pores because the pore impurities were cleaned by ethanol.

The pore size decreased after pillarization with pore diameters for Ti/NBR Clay, Ni-Ti/NBR Clay, and Co-Ti/NBR Clay, which are 40.4 Å, 41.3 Å, and 39.9 Å, respectively, indicating that Ti pillars produced larger pore sizes. Adding Ni and Co doping does not significantly change the pores of the pillared clay. The decrease in the pore diameter of Ti-pillared clay compared with Clay and NBR Clay+EtOH signifies that the swelling process in the clay layer does not occur in the pillared clay any more. Pillarization of clay by Ti^{4+} causes the swelling ability of the clay to decrease because Ti^{4+} binds between layers of clay and reduces the distance between layers of clay. This phenomenon is proven by the shift of peak d_{001} at $<10^\circ 2\theta$ toward a smaller 2θ value, indicating a narrowing of the interlayer distance and swelling of the clay. On the other hand, adding ethanol to clay causes the surface area and pore volume to decrease. This is due to the non-opening of the interlayer region, as shown by the lack of a d_{001} peak at $<10^\circ 2\theta$.

The surface area and pore volume of Ti/NBR Clay are almost the same as Co-Ti/NBR Clay, but what is interesting is that for Ni-doped on Ti-pillared clay, the surface area and pore volume increase and are greater than Ti/NBR Clay and Co-Ti/NBR Clay. The large surface area and pore volume may be because NiO is more evenly distributed in the pillared clay.

Table 1. Specific surface area (S_{BET}), pore volume (V_{T}), and pore diameter (d) of the samples

Sample	S_{BET} ($\text{m}^2 \text{g}^{-1}$)	V_{T} ($\text{cm}^3 \text{g}^{-1}$)	d (Å)
Clay	46.01	0.063	54.09
Clay+EtOH	37.97	0.056	58.55
Ti/NBR Clay	74.28	0.075	40.39
Ni-Ti/NBR Clay	85.25	0.09	41.34
Co-Ti/NBR Clay	75.59	0.076	39.87

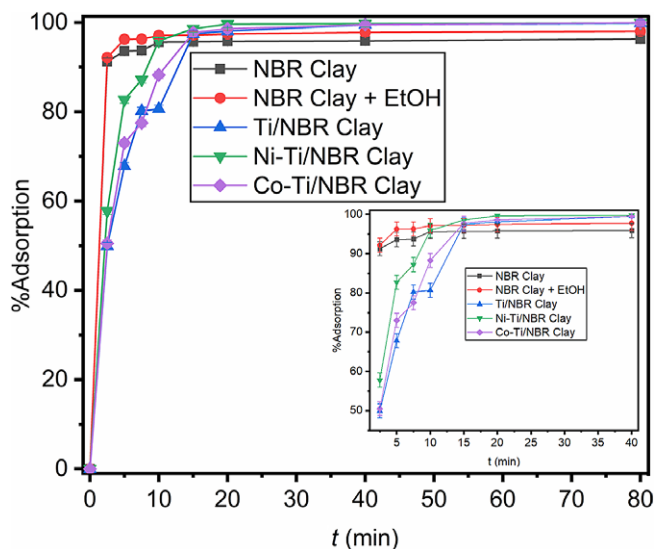


Figure 7. The adsorption (%) of RhB in Clay, Clay+EtOH, Ti/NBR Clay, Ni-Ti/NBR Clay, and Co-Ti/NBR Clay. Adsorption was carried out at room temperature with an RhB concentration of 40 mg L⁻¹. The inset explains the adsorption process over shorter times for clarity.

RhB adsorption

In general, porous materials have the potential to adsorb, especially macromolecules. This adsorption study was necessary because it contributes to our knowledge about the removal of RhB. Adsorption is influenced by several factors, such as the adsorbent's pore size, the adsorbate's size, and the adsorbate's or adsorbent's charge (Liu et al., 2019; Huang and Yang, 2020). The adsorption of the RhB solution is shown in Fig. 7.

The adsorption percentages by the NBR Clay and NBR Clay +EtOH show significant increases from 0 to 2.5 min with adsorptions of 91.27 and 92.15%, respectively. NBR Clay and NBR Clay+EtOH show the greatest adsorption at 80 min at 96.32 and 98.02%, respectively, while Ti/NBR Clay, Ni-Ti/NBR Clay, and Co-Ti/NBR Clay are optimum at 15 min with adsorption levels of 97.45, 98.56, and 97.74%, respectively; the greatest degrees of adsorption achieved were 99.83, 99.91, and 99.93%, respectively. At 2.5 min, the NBR Clay and NBR Clay+EtOH showed much greater adsorption than the Ti/NBR Clay, Ni-Ti/NBR Clay, and Co-Ti/NBR Clay. This could be due to the larger pore sizes of the NBR Clay and NBR Clay +EtOH than the Ti/NBR Clay, Ni-Ti/NBR Clay, and Co-Ti/NBR Clay so that the RhB molecule enters the pores quickly and shows significant adsorption within the first minute. This contrasts with Ti/NBR Clay, Ni-Ti/NBR Clay, and Co-Ti/NBR Clay, which have tiny pores despite their large pore volume and large surface area, resulting in significant adsorption even though the adsorption rate is slower.

Adsorption isotherms and thermodynamic

The adsorption model of RhB on clay was examined with several models, such as Langmuir, Freundlich, and Temkin (Table S1 in the Supplementary material) (Pareek et al., 2019). The Langmuir isotherm graph of RhB in the sample is shown in Fig. 8. The Langmuir isotherm adsorption model has a correlation coefficient (r) >0.99, which indicates that the Langmuir isotherm model is the most suitable at representing the adsorption. The Langmuir model is used for adsorption processes in which the adsorbate-adsorbent interaction is specific, and all the active sites are energetically equivalent; therefore, the process is considered to be

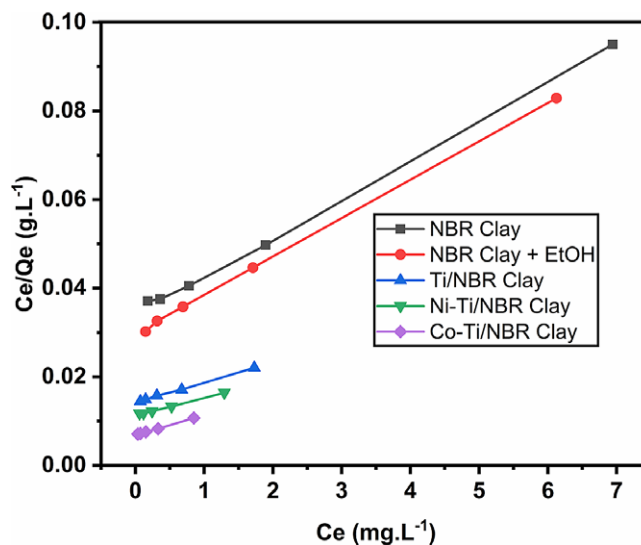


Figure 8. Langmuir isotherm curve of RhB on the surface of the adsorbent.

homogeneous (Bernal et al., 2018). The Langmuir isotherm adsorption equation is as follows:

$$\frac{C_e}{Q_e} = \frac{1}{bQ_{\max}} + \frac{C_e}{Q_{\max}}, \quad (1)$$

where C_e is the equilibrium concentration (mg L⁻¹), Q_e is the adsorbed capacity, Q_{\max} is the monolayer coverage of adsorbed RhB (mg g⁻¹), and b is the Langmuir constant (L mg⁻¹). The $\frac{C_e}{Q_e}$ vs C_e plot produces a straight line, and the Q_{\max} is obtained from the gradient plot, while b is obtained from the intercept plot.

The thermodynamics study of the adsorption of RhB on clay is viewed from the point of view of the Gibbs free energy ($\Delta G^{\circ}_{\text{ads}}$). The Gibbs free energy of adsorption can be determined from the K_0 using the following equation:

$$K_0 = \frac{Q_e}{C_e} \quad (2)$$

$$\Delta G^{\circ}_{\text{ads}} = -RT \ln K_0, \quad (3)$$

where Q_e is the surface concentration of RhB, K_0 is the thermodynamic equilibrium constant, R is the gas constant ($R=8.314 \text{ J mol}^{-1} \text{ K}^{-1}$), and T is the thermodynamic temperature ($T=298\text{K}$) (Khalaf et al., 2020). The values of b , Q_{\max} , K_0 , and $\Delta G^{\circ}_{\text{ads}}$ of RhB adsorption on the adsorbent are shown in Table 2. The b , K_0 , and $\Delta G^{\circ}_{\text{ads}}$ showed the largest results for Co-Ti/NBR Clay and the lowest on clay. The b and K_0 is a manifestation of the adsorption activity of the adsorbent, where the greater the value of b and K_0 , the greater the adsorption. The $\Delta G^{\circ}_{\text{ads}}$ also indicates the adsorption energy where the more negative the $\Delta G^{\circ}_{\text{ads}}$, the greater the adsorption. Note that values of $\Delta G^{\circ}_{\text{ads}}$ that are close to 20 kJ mol⁻¹ or less are compatible with physisorption, while values of ~40 kJ mol⁻¹ or more are compatible with chemisorption (Mourya et al., 2015). In this study, the $\Delta G^{\circ}_{\text{ads}}$ for all samples were <20 kJ mol⁻¹, indicating that the adsorption mechanism of RhB on the sample surface is classified as a physisorption mechanism.

The results of surface analysis (Table 1) indicate that the pore diameter values for NBR Clay+EtOH and NBR Clay significantly exceed those of Ti/NBR Clay, Ni-Ti/NBR Clay, and Co-Ti/NBR

Table 2. Langmuir parameters Q_{\max} , K_0 , and $\Delta G^{\circ}_{\text{ads}}$ from the adsorption of RhB on the adsorbent prepared at 298K

Sample	Q_{\max}	b	K_0	ΔG°
Clay	113.76	0.26	21.77	-7.4
Clay+EtOH	114.94	0.29	25.22	-7.75
Ti/NBR Clay	219.78	0.32	60.6	-9.86
Ni-Ti/NBR Clay	256.41	0.34	77.46	-10.45
Co-Ti/NBR Clay	218.34	0.66	124.94	-11.6

Table 3. Pseudo-second order reaction kinetic parameters of RhB on the adsorbent

Sample	k_2 ($\text{g mol}^{-1} \text{min}^{-1}$)	q_2 (mol g^{-1})	R
Clay	2410.75	0.0518	0.999
Clay+EtOH	2759.72	0.0509	0.999
Ti/NBR Clay	213.18	0.0485	0.999
Ni-Ti/NBR Clay	245.73	0.0487	0.999
Co-Ti/NBR Clay	430.92	0.0492	0.999

Clay, thereby accounting for their increased adsorption activity. Despite the opposing outcomes observed in S_{BET} and V_{T} values, the adsorption values consistently align with the trends in pore diameter (d). A larger d value facilitates the easy ingress of RhB molecules into the clay pores, consequently resulting in increased adsorption values. These findings further substantiate the rationale behind the greater adsorption values observed in Ni-Ti/NBR Clay compared with Ti/NBR Clay and Co-Ti/NBR Clay.

Adsorption kinetics

The adsorption kinetics of RhB by NBR Clay, NBR Clay+EtOH, Ti/NBR Clay, Co-Ti/NBR Clay, and Ni-Ti/NBR Clay can be represented by pseudo-first order and pseudo-second order. The pseudo-first order and pseudo-second order kinetic models are expressed in the following equations:

Pseudo-first order:

$$\frac{1}{q_t} = \left(\frac{k_1}{q_1}\right) \left(\frac{1}{t}\right) + \frac{1}{q_1} \quad (4)$$

Pseudo-second order:

$$\frac{t}{q_t} = \left(\frac{1}{q_2}\right) t + \frac{1}{k_2 \cdot q_2^2}, \quad (5)$$

where q_t is the adsorption capacity of RhB at a certain time (mol g^{-1}) at various times, t (min); q_1 is the maximum adsorption capacity (mol g^{-1}) for pseudo-first order adsorption, k_1 is the pseudo-first order rate constant for adsorption process (min^{-1}), q_2 is the maximum adsorption capacity (mol g^{-1}) for pseudo-second order adsorption, and k_2 is the rate constant pseudo-second order for adsorption ($\text{g mol}^{-1} \text{min}^{-1}$). The $\frac{1}{q_t}$ vs $\frac{1}{t}$ plot is used for pseudo-first order equations, while the $\frac{t}{q_t}$ vs t plot is for pseudo-second order equations (Fig. S2 in the Supplementary material). Based on the applied adsorption kinetics model, the pseudo-second order adsorption kinetics model has a correlation coefficient (R) closest

to 1 (Table S2 in the Supplementary material). These values indicate that the kinetic route of RhB adsorption on the sample surface follows a pseudo-second order kinetic model. The values of k_2 and q_2 calculated from these equations are shown in Table 3.

The value of the rate constant (k_2) and maximum adsorption capacity (q_2) of Co-Ti/NBR Clay > Ni-Ti/NBR Clay > Ti/NBR Clay, where these results are linear with the adsorption energy. The k_2 and q_2 of Clay and NBR Clay+EtOH are greater than those of Ti/NBR Clay, Ni-Ti/NBR Clay, and Co-Ti/NBR Clay, even though the adsorption energy values are smaller. This phenomenon can occur because the pore size of NBR Clay and NBR Clay+EtOH is larger than those of Ti/NBR Clay, Ni-Ti/NBR Clay, and Co-Ti/NBR Clay, so RhB molecules are absorbed much more quickly. The molecular size of RhB is 1.44 nm, and the pore size of Clay and NBR Clay+EtOH is four times as large, while Ti/NBR Clay, Ni-Ti/NBR Clay, and Co-Ti/NBR Clay are only three times as large as RhB (Huang et al., 2008).

RhB photodegradation

The photocatalytic degradation process was carried out by dispersing titania-pillared clay doped with nickel and cobalt into the RhB solution, incubated in the dark, and then irradiated with a UV lamp (Fig. 9). The treatment without UV radiation (dark) was carried out for 10 min, which is the adsorption saturation point, so it is considered that adsorption has no effect on RhB removal and only photocatalytic degradation activity has an effect (Helali et al., 2011). Based on Fig. 9, the optimum point of RhB degradation occurred at 40 min, where the RhB degradation of all samples exhibits almost the same value at 40 min. The percentage of degradation shows an increase in the removal of RhB compared with the percentage of adsorption, which proves the occurrence of photocatalytic degradation.

Kinetics of RhB photodegradation

Kinetic models of degradation of RhB solutions with nickel- and cobalt-doped titania-pillared clay samples in aqueous solutions were investigated. The reaction rate (R , $\text{mg L}^{-1} \text{min}^{-1}$) of degradation is expressed as follows:

$$R = \frac{kKC_e}{1 + KC_e}, \quad (6)$$

where C_e is the concentration of RhB (mg L^{-1}), k is the reaction rate constant, and K is the adsorption coefficient of RhB (L mg^{-1}). For lower initial concentrations of RhB, such as in ppm, the equation can be simplified by means of a first-order equation (El-Sharkawy et al., 2007). The first-order Langmuir-Hinshelwood equation is expressed as follows:

$$\ln \frac{C_0}{C_t} = k_{\text{app}} t, \quad (7)$$

where C_0 and C_t are RhB concentrations before and after irradiation (mg L^{-1}), t is the irradiation time (min), and k_{app} is the degradation rate constant (min^{-1}) (Alakhras et al., 2020). The $\ln \frac{C_0}{C_t}$ vs t plot (Fig. 10) gives a straight line with $R > 0.9$, indicating that the photocatalytic degradation of RhB follows first-order kinetics. The resulting line gradient shows the value of the degradation rate constant (k_{app}) of RhB.

The degradation rate constant (k_{app}) of RhB solution from Co-Ti/NBR Clay (0.0779 min^{-1}) > Ti/NBR Clay (0.0556 min^{-1}) > Ni-Ti/NBR Clay (0.0395 min^{-1}) > NBR Clay (0.0291 min^{-1}) > NBR

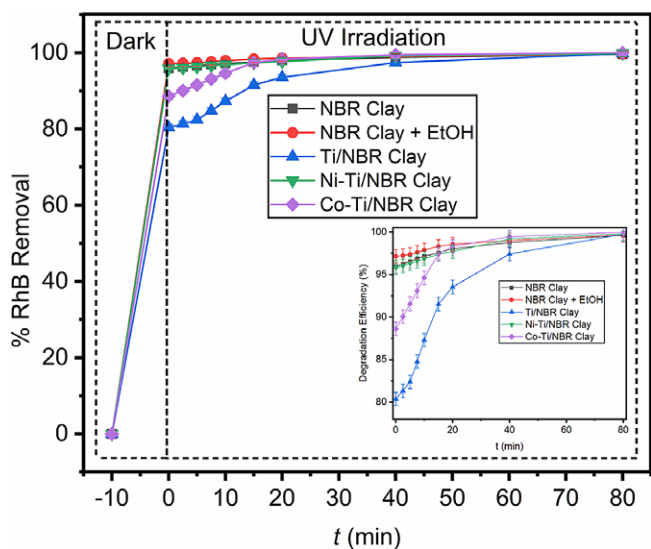


Figure 9. Degradation (%) of RhB solution with Clay, Clay+EtOH, Ti/NBR Clay, Ni-Ti/NBR Clay, and Co-Ti/NBR Clay in UV radiation. The application test was carried out using a 40 ppm RhB solution.

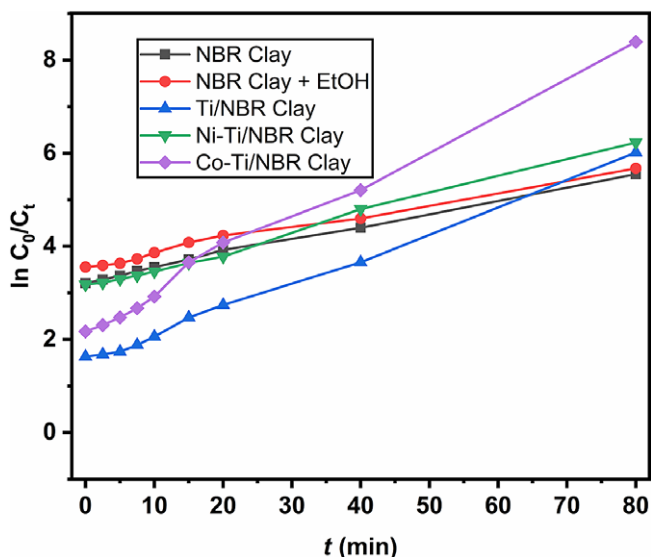


Figure 10. Plotted curve $\ln \frac{C_0}{C_t}$ vs t of Clay, Clay+EtOH, Ti/NBR Clay, Ni-Ti/NBR Clay, and Co-Ti/NBR Clay.

Clay+EtOH (0.0265 min^{-1}). The Ti/NBR Clay, Ni-Ti/NBR Clay, and Co-Ti/NBR Clay showed more significant photocatalytic activity for degrading RhB solutions than NBR Clay and NBR Clay+EtOH. It also shows that the Co-Ti/NBR Clay has the best photocatalytic activity compared with other samples. The rate constants of degradation of Ti/NBR Clay, Ni-Ti/NBR Clay, and Co-Ti/NBR Clay are greater than those of NBR Clay and NBR Clay+EtOH, which indicates that Ti-pillared clay can enhance photocatalytic activity. Such structures can capture photo-induced electrons and inhibit further recombination of electrons and holes. Thus, it can enhance the photocatalytic activity of photocatalysts to a large extent (Yang et al., 2004). In addition, with Co doping, the k_{app} increases. Metal doping can reduce the bandgap so that electrons from the valence band move easily to the conduction band, and RhB is more easily degraded. However, Ni-Ti/NBR Clay has a smaller k_{app} than Ti/NBR Clay. This

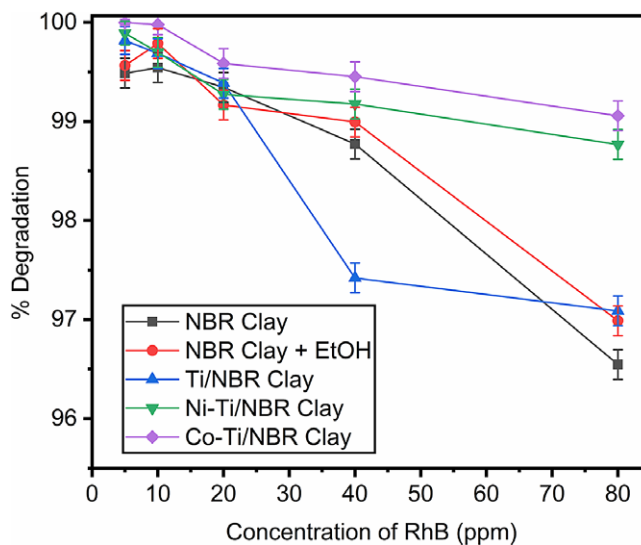


Figure 11. Photodegradation of RhB by UV light-irradiated samples. Photodegradation was carried out at room temperature for 40 min.

phenomenon could be due to the predominance of Ni-Ti/NBR Clay adsorption activity, so the photocatalytic degradation activity was not monitored clearly.

Photodegradation at various concentrations of RhB

Application tests were carried out by photocatalytic degradation of Rhodamine solution at various concentrations (5, 10, 20, 40, and 80 ppm). The results of the photocatalytic degradation of the RhB solution are presented in Fig. 11. In general, all samples showed decreased degradation ability with increasing RhB concentration. The greater the concentration, the more RhB molecules that must be degraded. With the same amount of catalyst, an increase in RhB concentration decreases the degradation percentage. In the NBR Clay and NBR Clay+EtOH, there was an increase in degradation from the RhB concentration of 5 to 10 mg L^{-1} . The Clay and NBR Clay+EtOH had little or no photocatalytic activity, as evidenced by the RhB removal value, i.e. there was little difference between photocatalytic adsorption and degradation. Most of the RhB removal results can be considered contributions from the adsorption activity of NBR Clay and NBR Clay+EtOH, and the RhB concentration of 10 mg L^{-1} is the adsorption saturation point. NBR Clay and NBR Clay+EtOH experienced a significant decrease in the percentage of degradation at RhB concentrations above 40 mg L^{-1} . Meanwhile, the degradation percentage for Ni-Ti/NBR Clay and Co-Ti/NBR Clay at RhB concentrations above 40 mg L^{-1} tended to be constant. These results indicate the contribution of photocatalytic activity due to the presence of Ni and Co metals as doping.

In addition, the difference in degradation percentage between NBR Clay and NBR Clay+EtOH and the Ni-Ti/NBR Clay and Co-Ti/NBR Clay at an RhB concentration of 80 mg L^{-1} was $\sim 2.14\%$. These phenomena indicate that at high RhB concentrations ($C_{RhB} > 40 \text{ mg L}^{-1}$), photocatalytic activity is more visible and predominates. The percentage degradation of the Ti/NBR Clay also decreased with increasing RhB concentration and decreased drastically when the RhB concentration was 20 mg L^{-1} to 40 mg L^{-1} of 1.97%. The Ti/NBR Clay has a much smaller pore size than the other samples, so the adsorption ability is small, and the RhB removal is also small. Like the Ni-Ti/NBR Clay and Co-Ti/NBR Clay, the Ti/NBR Clay also showed a constant degradation percentage at RhB concentrations from 40 to 80 mg L^{-1} . At an

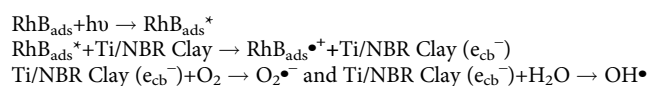
RhB concentration of 80 mg L⁻¹, the degradation percentage was 97.09%, greater than NBR Clay and NBR Clay+EtOH. This phenomenon indicates the contribution of the photocatalytic activity of the Ti/NBR Clay.

Mechanism of photocatalytic degradation

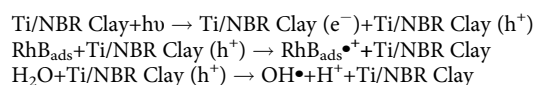
The photocatalytic degradation mechanism of RhB solution on titania-pillared clay samples and doped with Ni and Co metals was studied. Titania, a semiconductor metal, has photocatalytic activity when irradiated by UV (Wold, 1993). Adding Ni and Co metals as doping agents also increases the photocatalytic activity. The presence of doping can reduce the bandgap of titanium so that electrons from the valence band move easily to the conduction band (Guan et al., 2020).

The degradation of colored solutions by light can be divided into three mechanisms: (1) a photolysis process induced by light energy from a light source; (2) the photosensitization process, in which light irradiation excites electrons to the conduction band along with the oxidation of the dye; and (3) a proper heterogeneous photocatalytic process in which the promotion of electrons from the valence band to the conduction band produces holes for the oxidation of the dye (Martínez-de la Cruz et al., 2010). RhB solution is stable for a long time so that the photolysis process can be ignored. The mechanism of RhB degradation in Ti/NBR Clay, Ni-Ti/NBR Clay, and Co-Ti/NBR Clay is dominated by photosensitization and photocatalytic processes:

Photosensitization process (Zhao et al., 2008):



Photocatalytic process (Wilhelm et al., 2007):



Then, species such as O₂^{•-} and OH[•] react with RhB species, and degradation occurs: RhB_{ads}^{•+} (O₂^{•-} or OH[•]) → degradation → CO₂+H₂O.

Conclusions

Titania-pillared clays embedded with nickel and cobalt have been synthesized successfully. The synthesis of titania-pillared clay doped with nickel and cobalt from clay does not change the functional groups of the clay, such as Si-OH and Al-OH. XRD results show that TiO₂ can become a pillar and cause the distance between layers to be larger. There was an increase in surface area and pore volume with TiO₂ pillaring doped with Ni²⁺ and Co²⁺, while the pore size tended to be more constant. TGA results show that all samples are stable up to 650°C, except for Co-Ti/NBR Clay. The adsorption of NBR Clay and NBR Clay+EtOH showed a greater adsorption rate constant than Ti/NBR Clay, Ni-Ti/NBR Clay, and Co-Ti/NBR Clay. Nonetheless, the adsorption energy of Ti/NBR Clay, Ni-Ti/NBR Clay, and Co-Ti/NBR Clay is more prominent than that of NBR Clay and NBR Clay+EtOH. All samples followed the Langmuir isotherm model with a physisorption mechanism. TiO₂ splinting in clay can increase photocatalytic degradation activity, while nickel and cobalt doping further increase photocatalytic degradation activity. With increasing RhB concentration, the photodegradation performance was slightly reduced. This research serves as a valuable reference for

the development of clay composites with effective dye-removal capabilities. The study yields notable results, showcasing a high RhB removal activity driven primarily by adsorption. However, the excessive adsorption of clay hindered a thorough observation of the photodegradation activity of the composite. Future research endeavors could prioritize investigations into photodegradation activity, employing suitable experimental methods and standardization techniques to facilitate accurate observations. Moreover, there is potential to explore a co-doping mechanism with two metals, aiming to enhance the photodegradation activity of the composite.

Supplementary material. The supplementary material for this article can be found at <http://doi.org/10.1017/cmn.2024.12>.

Author contributions. **Adi Darmawan:** Conceptualization; Methodology; Validation; Formal Analysis; Resources; Writing-review & editing; Supervision; Funding acquisition. **Setyo Sulaksono:** Methodology; Investigation; Formal analysis. **Muhamad Samsul Arifin:** Methodology; Investigation; Formal analysis. **Hasan Muhtar:** Formal analysis; Investigation; Data curation; Writing-original draft; Visualization. **Sriyanti Sriyanti:** Validation; Writing-review & editing; Supervision.

Acknowledgments. Adi Darmawan is very grateful to FIM2lab at the University of Queensland, which facilitated all FTIR, TGA, and GSA analyses.

Financial support. Adi Darmawan gratefully acknowledges the financial support provided by Diponegoro University via Indonesian Collaborative Research (RKI) Based on Decree Number 1618/IT1.B07.1/TA.00/2022 and Agreement/Contract Number 434-01/UN7.D2/PP/VI/2022 dated 14 June 2022.

Competing interest. The authors declare that they have no competing interests.

Data availability statement. Data is available within the article, and no additional information is provided.

References

- Abdo Segne, T., Rao Tirukkavalluri, S., & Challapalli, S. (2011). Studies on characterization and photocatalytic activities of visible light sensitive TiO₂ nano catalysts co-doped with magnesium and copper. *International Research Journal of Pure and Applied Chemistry*, 1, 84–103. <https://doi.org/10.9734/IRJPAC/2011/453>
- Ahmad, N., Hussain, S.T., Muhammad, B., Ali, N., Abbas, S.M., & Ali, Z. (2013). Zr-pillared montmorillonite supported cobalt nanoparticles for Fischer-Tropsch synthesis. *Progress in Natural Science: Materials International*, 23, 374–381. <http://doi.org/10.1016/j.pnsc.2013.06.010>
- Alakhras, F., Alhajri, E., Haounati, R., Ouachtak, H., Addi, A.A., & Saleh, T.A. (2020). A comparative study of photocatalytic degradation of Rhodamine B using natural-based zeolite composites. *Surfaces and Interfaces*, 20, 100611. <https://doi.org/10.1016/j.surfin.2020.100611>
- ALothman, Z.A. (2012). A review: fundamental aspects of silicate mesoporous materials. *Materials*, 5, 2874–2902. <https://doi.org/10.3390/ma5122874>
- Bahranowski, K., Włodarczyk, W., Wisła-Walsh, E., Gawel, A., Matusik, J., Klimek, A., Gil, B., Michalik-Zym, A., Dula, R., Socha, R.P., & Serwicka, E. M. (2015)[Ti,Zr]-pillared montmorillonite – a new quality with respect to Ti- and Zr-pillared clays. *Microporous and Mesoporous Materials*, 202, 155–164. <https://doi.org/10.1016/j.micromeso.2014.09.055>
- Basumatary, R., Basumatary, B., Konwar, D., & Ramchiary, A. (2023). Tailored highly efficient Co-doped TiO₂/CoTiO₃ heterojunction photocatalyst for methylene blue degradation under visible light. *Journal of the Korean Ceramic Society*, 60, 547–559. <https://doi.org/10.1007/s43207-022-00284-z>
- Bernal, V., Giraldo, L., & Moreno-Piraján, J.C. (2018). Physicochemical properties of activated carbon: their effect on the adsorption of pharmaceutical compounds and adsorbate-adsorbent interactions. *C Journal of Carbon Research*, 4, 62. <https://doi.org/10.3390/c4040062>

- Borno, I.B., & Ashraf, W. (2023). Effects of co-calcining kaolinite-rich clay blends with alkali and alkali earth metal hydroxides. *Applied Clay Science*, 231, 106742. <https://doi.org/10.1016/j.clay.2022.106742>
- Cardona, Y., Węgrzyn, A., Miśkowiec, P., Korili, S.A., & Gil, A. (2022). Catalytic photodegradation of organic compounds using TiO_2 /pillared clays synthesized using a nonconventional aluminum source. *Chemical Engineering Journal*, 446, 136908. <https://doi.org/10.1016/j.cej.2022.136908>
- Costache, M.C., Heidecker, M.J., Manias, E., & Wilkie, C.A. (2006). Preparation and characterization of poly(ethylene terephthalate)/clay nanocomposites by melt blending using thermally stable surfactants. *Polymers for Advanced Technologies*, 17, 764–771. <https://doi.org/10.1002/pat.752>
- Dao, T.B.T., Ha, T.T.L., Nguyen, T.D., Le, H.N., Ha-Thuc, C.N., Nguyen, T.M.L., Perre, P., & Nguyen, D.M. (2021). Effectiveness of photocatalysis of mm-t supported TiO_2 and TiO_2 nanotubes for Rhodamine B degradation. *Chemosphere*, 280, 130802. <https://doi.org/10.1016/j.chemosphere.2021.130802>
- El-Sharkawy, E.A., Soliman, A.Y., & Al-Amer, K.M. (2007). Comparative study for the removal of methylene blue via adsorption and photocatalytic degradation. *Journal of Colloid and Interface Science*, 310, 498–508. <https://doi.org/10.1016/j.jcis.2007.02.013>
- El Mragui, A., Zegaoui, O., & da Silva, J.C.E. (2021). Elucidation of the photocatalytic degradation mechanism of an azo dye under visible light in the presence of cobalt doped TiO_2 nanomaterials. *Chemosphere*, 266, 128931. <https://doi.org/10.1016/j.chemosphere.2020.128931>
- Eren, E. (2010). Adsorption performance and mechanism in binding of azo dye by raw bentonite. *CLEAN – Soil, Air, Water*, 38, 758–763. <https://doi.org/10.1002/clen.201000060>
- Guan, B., Yu, J., Guo, S., Yu, S., & Han, S. (2020). Porous nickel doped titanium dioxide nanoparticles with improved visible light photocatalytic activity. *Nanoscale Advances*, 2, 1352–1357. <https://doi.org/10.1039/C9NA00760A>
- Helali, S., Puzenat, E., Perol, N., Safi, M.-J., & Guillard, C. (2011). Methylamine and dimethylamine photocatalytic degradation– adsorption isotherms and kinetics. *Applied Catalysis A: General*, 402, 201–207. <https://doi.org/10.1016/j.apcata.2011.06.004>
- Huang, J.-H., Huang, K.-L., Liu, S.-Q., Wang, A.T., & Yan, C. (2008). Adsorption of Rhodamine B and methyl orange on a hypercrosslinked polymeric adsorbent in aqueous solution. *Colloids and Surfaces A: Physicochemical and Engineering Aspects*, 330, 55–61. <https://doi.org/10.1016/j.colsurfa.2008.07.050>
- Huang, X., & Yang, G. (2020). Charge reversal and anion effects during adsorption of metal ions at clay surfaces: mechanistic aspects and influence factors. *Chemical Physics*, 529, 110575. <https://doi.org/10.1016/j.chemphys.2019.110575>
- Johnson, E.A., & Post, J.E. (2006). Water in the interlayer region of birnessite: importance in cation exchange and structural stability. *American Mineralogist*, 91, 609–618. <https://doi.org/10.2138/am.2006.2090>
- Karakassides, M.A., Gournis, D., & Petridis, D. (1999). An infrared reflectance study of Si–O vibrations in thermally treated alkali-saturated montmorillonites. *Clay Minerals*, 34, 429–438. <https://doi.org/10.1180/000985599546334>
- Khalaf, M.M., Tantawy, A.H., Soliman, K.A., & Abd El-Lateef, H.M. (2020). Cationic Gemini-surfactants based on waste cooking oil as new 'green' inhibitors for n80-steel corrosion in sulphuric acid: a combined empirical and theoretical approaches. *Journal of Molecular Structure*, 1203, 127442. <https://doi.org/10.1016/j.molstruc.2019.127442>
- Khan, M.D., Singh, A., Khan, M.Z., Tabraiz, S., & Sheikh, J. (2023). Current perspectives, recent advancements, and efficiencies of various dye-containing wastewater treatment technologies. *Journal of Water Process Engineering*, 53, 103579. <https://doi.org/10.1016/j.jwpe.2023.103579>
- Kumar, J., Mariappan, C.R., Kumar, V., Murugavel, S., & Prakash, G.V. (2016). Study of spinel-type $\text{ZnNi}_x\text{Co}_{2-x}\text{O}_4$ nano-particles, synthesised by thermal decomposition of ternary metal nitrate solutions. *Materials Research Bulletin*, 83, 632–639. <http://doi.org/10.1016/j.materresbull.2016.07.011>
- Laboureur, D., Glabeke, G., & Gouriet, J.B. (2019). Aluminum nanoparticles oxidation by tga/dsc. *Journal of Thermal Analysis and Calorimetry*, 137, 1199–1210. <https://doi.org/10.1007/s10973-019-08058-2>
- Li, Y., Cai, X., Guo, J., Zhou, S., & Na, P. (2015). Fe/Ti co-pillared clay for enhanced arsenite removal and photo oxidation under UV irradiation. *Applied Surface Science*, 324, 179–187. <http://doi.org/10.1016/j.apsusc.2014.10.111>
- Liu, J., Xie, H., Wang, Q., Chen, S., & Hu, Z. (2019). The effect of pore size on shale gas recovery with CO_2 sequestration: insight into molecular mechanisms. *Energy & Fuels*, 33, 2897–2907. <https://doi.org/10.1021/acs.energyfuels.8b04166>
- Martínez-de la Cruz, A., & Pérez, U.M.G. (2010). Photocatalytic properties of bivo, prepared by the co-precipitation method: degradation of Rhodamine B and possible reaction mechanisms under visible irradiation. *Materials Research Bulletin*, 45, 135–141. <https://doi.org/10.1016/j.materresbull.2009.09.029>
- Mourya, P., Singh, P., Tewari, A.K., Rastogi, R.B., & Singh, M.M. (2015). Relationship between structure and inhibition behaviour of quinolinium salts for mild steel corrosion: Experimental and theoretical approach. *Corrosion Science*, 95, 71–87. <https://doi.org/10.1016/j.corsci.2015.02.034>
- Najafi, H., Farajfa, S., Zolgharnian, S., Mirak, S.H.M., Asasian-Kolur, N., & Sharifian, S. (2021). A comprehensive study on modified-pillared clays as an adsorbent in wastewater treatment processes. *Process Safety and Environmental Protection*, 147, 8–36. <https://doi.org/10.1016/j.psep.2020.09.028>
- Nakata, K., & Fujishima, A. (2012). TiO_2 photocatalysis: design and applications. *Journal of Photochemistry and Photobiology C: Photochemistry Reviews*, 13, 169–189. <https://doi.org/10.1016/j.jphotochemrev.2012.06.001>
- Opra, D.P., Gnedenkov, S.V., Sinebryukhov, S.L., Gerasimenko, A.V., Ziatdinov, A.M., Sokolov, A.A., Podgorbunsky, A.B., Ustinov, A.Y., Kuryavyi, V.G., & Mayorov, V.Y. (2021). Enhancing lithium and sodium storage properties of TiO_2 (b) nanobelts by doping with nickel and zinc. *Nanomaterials*, 11, 1703. <https://doi.org/10.3390/nano11071703>
- Ouidri, S., & Khalaf, H. (2009). Synthesis of benzaldehyde from toluene by a photocatalytic oxidation using TiO_2 -pillared clays. *Journal of Photochemistry and Photobiology A: Chemistry*, 207, 268–273. <http://doi.org/10.1016/j.jphotochem.2009.07.019>
- Pareek, S., Jain, D., Hussain, S., Biswas, A., Shrivastava, R., Parida, S.K., Kisan, H. K., Lgaz, H., Chung, I.-M., & Behera, D. (2019). A new insight into corrosion inhibition mechanism of copper in aerated 3.5 wt.% NaCl solution by eco-friendly imidazopyrimidine dye: experimental and theoretical approach. *Chemical Engineering Journal*, 358, 725–742. <https://doi.org/10.1016/j.cej.2018.08.079>
- Pinnavaia, T.J. (1983). Intercalated clay catalysts. *Science*, 220, 365–371. doi: 10.1126/science.220.4595.365
- Santos, K.S., Lopes, P.A.L., Mascarenhas, A.J.S., & Silva, L.A. (2023). Photocatalytic removal of cyanide from cassava processing wastewater with simultaneous generation of H_2 and C_2H_4 using Ni-modified TiO_2 . *Waste and Biomass Valorization*, 14, 3869–3880. <https://doi.org/10.1007/s12649-023-02098-4>
- Sarier, N., Onder, E., & Ersoy, S. (2010). The modification of na-montmorillonite by salts of fatty acids: an easy intercalation process. *Colloids and Surfaces A: Physicochemical and Engineering Aspects*, 371, 40–49. <https://doi.org/10.1016/j.colsurfa.2010.08.061>
- Starink, M.J. (2003). The determination of activation energy from linear heating rate experiments: a comparison of the accuracy of isoconversion methods. *Thermochimica Acta*, 404, 163–176. [https://doi.org/10.1016/S0040-6031\(03\)00144-8](https://doi.org/10.1016/S0040-6031(03)00144-8)
- Sukhadeve, G.K., Janbandhu, S.Y., Kumar, R., Lataye, D.H., Ramteke, D.D., & Gedam, R.S. (2022). Visible light assisted photocatalytic degradation of indigo carmine dye and NO_2 removal by Fe doped TiO_2 nanoparticles. *Ceramics International*, 48, 29121–29135. <https://doi.org/10.1016/j.ceramint.2022.05.053>
- Sun, L., Zhai, J., Li, H., Zhao, Y., Yang, H., & Yu, H. (2014). Study of homologous elements: Fe, Co, and Ni dopant effects on the photoreactivity of TiO_2 nanosheets. *ChemCatChem*, 6, 339–347. <https://doi.org/10.1002/cctc.201300879>
- Tretiak, C.S., & Abdallah, N.B. (2009). Sorption and desorption characteristics of a packed bed of clay– CaCl_2 desiccant particles. *Solar Energy*, 83, 1861–1870. <https://doi.org/10.1016/j.solener.2009.06.017>
- Van Hoang, N., Nguyen-Thi, L., Kim, G.M., Dang, T.-D., Ngoc Toan, V., & La, D.D. (2022). Green synthesis of zero-valent iron nanoparticles by cleistocalyx operculatus leaf extract using microfluidic device for degradation of the Rhodamine B dye. *Advances in Natural Sciences: Nanoscience and Nanotechnology*, 13, 045007. <https://doi.org/10.1088/2043-6262/aca023>
- Wilhelm, P., & Stephan, D. (2007). Photodegradation of Rhodamine B in aqueous solution via $\text{SiO}_2/\text{TiO}_2$ nano-spheres. *Journal of Photochemistry and Photobiology A: Chemistry*, 185, 19–25. <https://doi.org/10.1016/j.jphotochem.2006.05.003>

- Wold, A. (1993). Photocatalytic properties of titanium dioxide (TiO₂). *Chemistry of Materials*, 5, 280–283. <https://doi.org/10.1021/cm00027a008>
- Yamanaka, S., Nishihara, T., Hattori, M., & Suzuki, Y. (1987). Preparation and properties of titania pillared clay. *Materials Chemistry and Physics*, 17, 87–101. [https://doi.org/10.1016/0254-0584\(87\)90050-2](https://doi.org/10.1016/0254-0584(87)90050-2)
- Yan, Y., Sun, J., Han, Y., Li, D., & Cui, K. (2010). Microstructure and bioactivity of Ca, P and Sr doped TiO₂ coating formed on porous titanium by micro-arc oxidation. *Surface and Coatings Technology*, 205, 1702–1713. <https://doi.org/10.1016/j.surfcoat.2010.09.040>
- Yang, Y., Li, X.-J., Chen, J.-T., & Wang, L.-Y. (2004). Effect of doping mode on the photocatalytic activities of Mo/TiO₂. *Journal of Photochemistry and Photobiology A: Chemistry*, 163, 517–522. <https://doi.org/10.1016/j.jphotochem.2004.02.008>
- Yusuf, M.O. (2023). Bond characterization in cementitious material binders using fourier-transform infrared spectroscopy. *Applied Sciences*, 13, 3353. <https://doi.org/10.3390/app13053353>
- Zhang, M., Li, M., Wang, Y., & Sun, J. (2022). Experimental study of thermal shrinkage and melt dripping properties of expanded polystyrene under various heat fluxes. *Journal of Building Engineering*, 60, 105179. <https://doi.org/10.1016/j.jobe.2022.105179>
- Zhang, P., Zhang, Z., Li, W., & Zhu, M. (2013). Effect of Ti-OH groups on microstructure and bioactivity of TiO₂ coating prepared by micro-arc oxidation. *Applied Surface Science*, 268, 381–386. <http://doi.org/10.1016/j.apsusc.2012.12.105>
- Zhang, W., Li, Q., & Xia, H. (2023). Photocatalytic oxidation of 5-hydroxymethylfurfural to furandicarboxylic acid over the Au-Ag/TiO₂ catalysts under visible light irradiation. *Applied Surface Science*, 613, 156036. <https://doi.org/10.1016/j.apsusc.2022.156036>
- Zhao, Y., Li, C., Liu, X., Gu, F., Du, H.L., & Shi, L. (2008). Zn-doped TiO₂ nanoparticles with high photocatalytic activity synthesized by hydrogen-oxygen diffusion flame. *Applied Catalysis B: Environmental*, 79, 208–215. <https://doi.org/10.1016/j.apcatb.2007.09.044>
- Zhirong, L., Azhar Uddin, M., & Zhanxue, S. (2011). FT-IR and XRD analysis of natural Na-bentonite and Cu(ii)-loaded Na-bentonite. *Spectrochimica Acta Part A: Molecular and Biomolecular Spectroscopy*, 79, 1013–1016. <https://doi.org/10.1016/j.saa.2011.04.013>
- Zhou, X., Qian, K., Zhang, Y., Li, D., Wei, Z., Wang, H., Ye, R., Liu, J., Ye, B., & Huang, W. (2020). Tuning the size of photo-deposited metal nanoparticles via manipulating surface defect structures of tio₂ nanocrystals. *Chemical Communications*, 56, 1964–1967. <https://doi.org/10.1039/C9CC09642F>
- Zhu, J., Zhu, L., Zhu, R., Tian, S., & Li, J. (2009). Surface microtopography of surfactant modified montmorillonite. *Applied Clay Science*, 45, 70–75. <http://doi.org/10.1016/j.clay.2009.04.010>